PROCEEDINGS, 45th Workshop on Geothermal Reservoir Engineering
Stanford University, Stanford, California, February 10-12, 2020
SGP-TR-216

Seismic Imaging of Spatial Heterogeneity at The Geysers Geothermal Reservoir Using a Cost-Effective Dense Seismic Network

Roland Gritto[1], Steve P. Jarpe[2], Lawrence J. Hutchings[2], Craig Ulrich[3], Corinne E. Layland-Bachmann[3], Martin Schoenball[3], Yves Guglielmi[3], Craig S. Hartline[4], Kurt T. Nihei[3], Seiji Nakagawa[3]

[1]Array Information Technology, 2020 Cedar Street, Berkeley, CA 94709

[2]Jarpe Data Solutions Inc., Prescott Valley, AZ 86314

[3]Lawrence Berkeley National Laboratory, Berkeley, CA 94720

[4]Calpine Corporation, Middletown, CA 95461

Roland.Gritto@arrayinfotech.com

Keywords: geothermal reservoir, dense seismic array, seismic reservoir imaging

ABSTRACT

In this paper, we present results of high-resolution seismic imaging using a cost-effective dense seismic network to image spatial heterogeneity of the reservoir structure and flow paths at The Geysers geothermal reservoir in northern California, USA. The project employs 91 seismic recording systems, spaced at approximately 500 m over a 5 km x 5 km study area. Seismic data for more than 17,000 earthquakes, over a period of one year, were acquired and automatically processed for P- and S-wave phase arrival times. The data were subsequently inverted using a joint inversion approach to image the spatial heterogeneity of the reservoir including the 3D P- and S-wave velocity structure and hypocenter locations. The resulting tomographic images are appraised by integration into The Geysers' 3D reservoir model and by spatial correlation to injection and production wells. Spatial correlation of P-wave velocity images to water injection and steam productions wells reveal higher velocities below injection wells, likely due to higher water saturation, and lower velocities in the vicinity of steam-producing wells, likely due to the presence of steam in the surrounding reservoir rocks. The spatial correlation of steam to production wells is highlighted in images of the Vp/Vs-ratio, which show decreased estimates in the vicinity of a group of steam production wells. This suggest that Vp/Vs-ratio is a useful parameter to estimate the spatial distribution of steam in the reservoir.

1. INTRODUCTION

In recent past, the availability of inexpensive seismic recording systems has led to the use of passive seismic networks with dense station coverage to investigate shallow and deeper structures of the Earth's crust. The resulting high-density seismic data sets have been used to, i.e., assess seismic hazard in the Los Angeles Basin (Bowden et al., 2015), to perform high-resolution imaging of the fault structure below Long Beach (Lin et al., 2013; Nakata et al., 2015), to investigate the magmatic resource of Mount St. Helens (Wang et al., 2017) and to investigate the structural controls of the Upper Rhein Graben near the Soultz-sous-Forêts and Rittershoffen geothermal reservoirs (Lehujeur, 2018). While the use of passive seismic networks with dense station coverage is only emerging as a tool to gain high-fidelity insight into the structural controls of geothermal reservoirs, commercial utilization of this technique is commonplace and includes monitoring of hydraulic fractures in oil and gas exploration. (i.e., MicroSeismic; FairfieldNodal; NodalSeismic). Considering the natural occurrence of micro-seismicity during geothermal operations, passive seismic networks with dense station coverage utilizing inexpensive recoding systems offer cost-effective strategies to investigate with high-resolution the structural controls of the reservoir. This will enable geothermal operators to more efficiently carry out their operations, including drilling productive wells, avoiding drilling hazards, and optimizing production. In the current paper, we present results of a seismic imaging study in the northwest Geysers geothermal reservoir using the temporary deployment of cost-effective three-component seismic sensors.

2. COST-EFFECTIVE DENSE SEISMIC NETWORK

The cost-effective dense-seismic network, that was installed in The Geysers in the spring of 2018, is comprised of recording systems designed by Jarpe Data Solutions Inc. (JDS). The seismic station is housed in a 30 x 25 x 10 cm sized box with a 10 W solar panel as shown in Figure 1. It comprises three orthogonally oriented 4.5 Hz geophones, a 12 V battery, an electric circuit board with two SD memory card slots, delta-sigma 24-bit digitization, a GPS antenna, continuous data recording and has 360 mW power consumption. Metal fins are connected to the outside of the enclosure and extend into concrete pads for improved ground coupling as shown in Figure 1.

The original goal of the network design was a temporary deployment of 100 stations with 500 m station spacing over a study area of 5 km x 5 km in the northwest Geysers (Figure 2a). In a recent study, Gritto et al. (2019) showed that a dense seismic network with regularly spaced stations is not required to achieve good resolution of the seismic properties in the reservoir at depth. A dense network with the same number of stations randomly distributed over the same region will yield comparable resolution, while the difference between these network configurations is confined to the shallow depth below the stations. This result is advantageous at The Geysers because the extreme topography and vegetation coverage prevents a regular-spaced station deployment. The network deployment was done over a three-week period in April/May 2018, when 91 stations were sited. Nine stations could not be deployed due to excessive vegetation coverage or inaccessibility of the originally planned locations. The final locations of the network stations are presented in Figure 2b. It can be seen that despite the challenging environment, the network stations reveal a high degree of regular spacing at approximately 500 m offset. The data retrieval interval was three months, which is longer than for most nodal-type stations. Because the current project is supported by the California Energy Commission (CEC), the temporary station will subsequently be referred to as "CEC" stations.

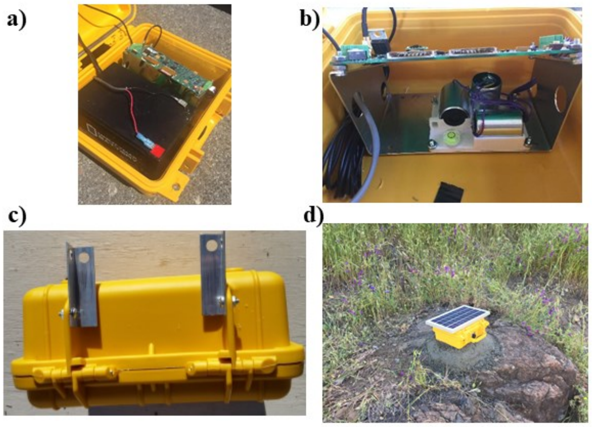

Figure 1: a) Interior of seismic station with battery and electronic circuit board. b) One-piece metal bracket with electronic circuit board (top) and three orthogonally oriented geophone components (bottom). c) Metal fins attached to outside of water-tight enclosure to improve coupling to concrete pad. d) Seismic station located on rock outcrop.

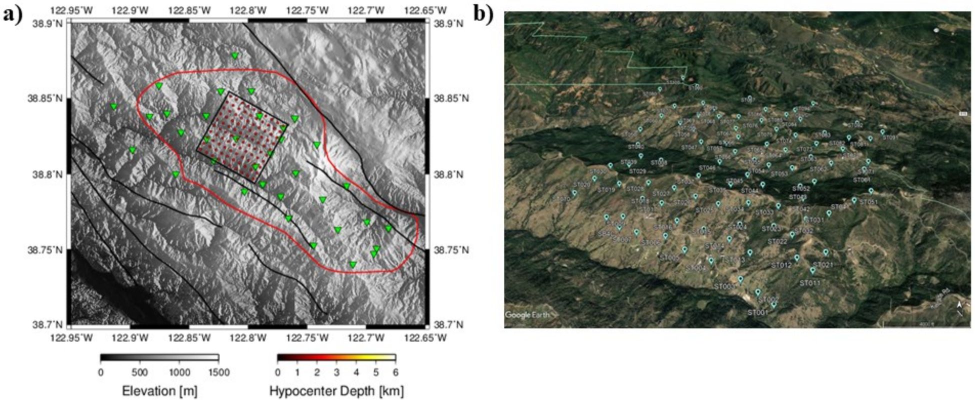

Figure 2: a) Map showing the outline of the Geysers steam field (red polygon), the permanent seismic BG network (green triangles), and the 5 km x 5 km study area (black square) with the planned locations of the temporary CEC stations (red dots). b) Final network configuration of the 91 CEC stations throughout the study area in northwest Geysers.

3. SEISMIC DATA PROCESSING

3.1 Data Quality Assessment

Of the 91 CEC stations, five were co-located with stations of the permanent seismic (BG) network that has been operating at The Geysers for over 20 years. The co-located stations allowed us to evaluate the quality of recorded data between the permanent and the temporary stations (Layland-Bachmann et al., 2019). The following example summarizes the appraisal of sensor performance using waveforms generated by a magnitude Mw=1.0 event and recorded by stations CECSB4 (temporary CEC station) and BGSB4 (permanent BG network station), which are co-located along the south-western margin of the 5 km x 5 km study area. Data evaluation was performed in the time and spectral domain, after waveforms were corrected by the instrument responses of the two seismic recording systems. The waveforms generated by the Mw=1.0 event are presented in Figure 3. The figure illustrates the waveforms recorded by the CEC station in red superimposed on those recorded by the permanent BG station in black. It can be seen that the waveforms reveal a good fit not only for the P- and S-wave phases but also for the noise and scattered phases throughout the traces.

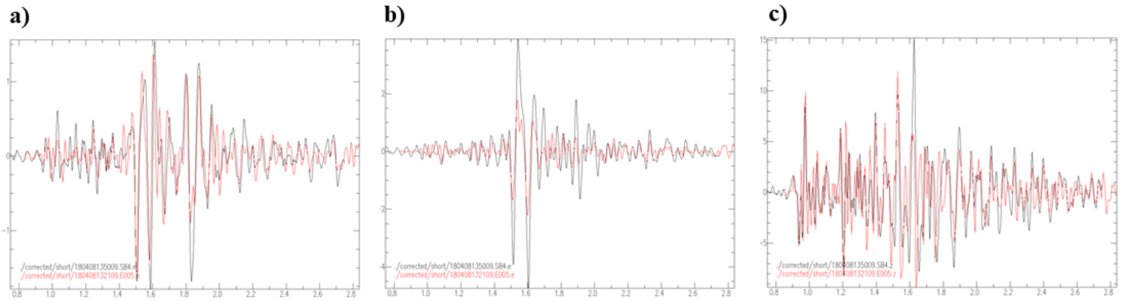

Figure 3: Seismic waveforms recorded by the temporary network station CECSB4 (red) and by the permanent BG station BGSB4 (black) for an earthquake with moment magnitude Mw=1.0. a) north component. b) east component. c) vertical component.

The amplitude spectra of the recorded waveforms in Figure 3 are presented in Figure 4. The spectra include the three components of the temporary station CECSB4 (red) and of the permanent station BGSB4 (black). The spectra reveal the same shape over the frequency range from 0.01 to 100 Hz, with similar amplitudes from the noise level at 1 Hz to the maxima at 10 Hz and for the fall-off from 10 to 100 Hz. However, between 1 and 10 Hz, the temporary station CGSB4 reveals slightly lower amplitudes than station BGSB4.

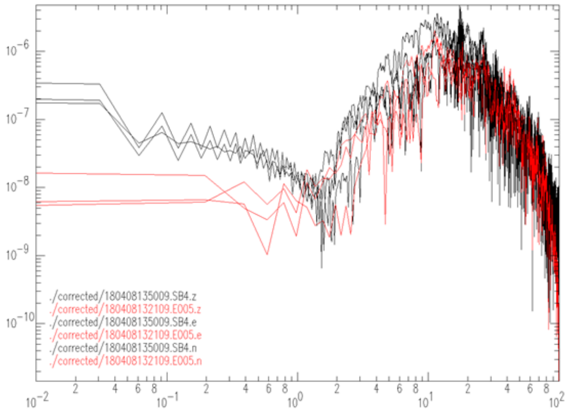

Figure 4: Amplitude spectra of the north-, east- and vertical-component recorded by the temporary CEC station CGSB4 (red) and by the permanent BG station BGSB4 (black) for the Mw=1.0 event.

Overall it can be stated that the co-located stations show good agreement in the recorded waveforms and the spectral content of the seismic waves particularly for an earthquake of magnitude Mw=1.0. The station evaluation by Layland-Bachmann et al., (2019) was performed for different sized earthquakes at different co-located stations (not shown here). That study also concluded that the temporary CEC network records more events at smaller magnitudes compared to the permanent BG network, due to the denser station spacing of the former. The results gave us confidence that the seismic data recorded by the temporary CEC network is representative of the seismic wavefield generated by earthquakes in the study area and that they can be used for seismic imaging of reservoir properties.

3.2 Data Processing

Seismic data processing is performed by Jarpe Data Solutions, Inc. (JDS), based on the REMAS software, which performs fast, automated processing of micro-earthquake data from dense networks. This code provides complete data processing including phase detection, event association and preliminary event location, estimation of phase travel time, pulse width, and event moment magnitude and energy release, generation of waveforms and storage of parameters in a database. The workflow consists of various processes that are executed sequentially from the raw data to the final seismic products that are subsequently used to analyze micro-seismic event locations and to image seismic velocities and attenuation in the reservoir. The first 13 months of processed data resulted in over 17,000 events and included over 600,000 P-wave phase arrivals and more than 500,000 S-wave phase arrival. The magnitudes of the 17,000 events ranged from $0 \leq Mw \leq 3$, with the maximum number of events observed at Mw = 0.4 (Figure 5a). The relocated earthquakes resulting from the 3D inversion are presented in Figure 5b. The figure shows the 5 x 5 km study area indicated by the green square, the 91-station CEC network represented by the cyan-colored triangles and the 17,000 earthquakes, color-coded for hypocentral depth. It can be seen that the events cover a much wider region beyond the study area and range from 0 km to 6 km depth. While there exists a mix of shallow and deep events in the reservoir below the study area, the seismicity reveals a general trend from shallower events in the south-east to deeper events in the north-west. This trend is a manifestation of the extent of the geothermal reservoir to greater depth towards the north-west.

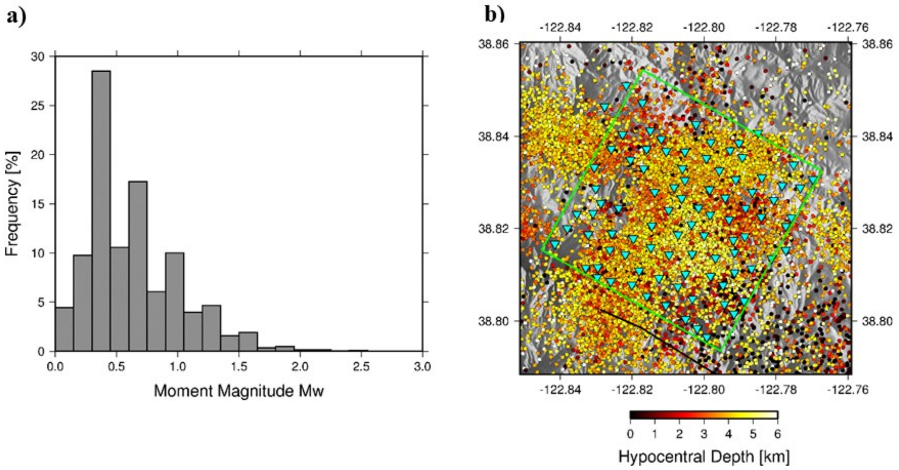

Figure 5: a) Histogram with moment magnitude (Mw) distribution for the set of 17,000 events. b) Map view of relocated seismicity resulting from 3D tomographic inversion of P- and S-wave travel time data. The seismicity represent 17,000 events recorded between May 2018 and June 2019.

4. SEISMIC RESERVOIR IMAGING

4.1 P- and S-Wave Velocity Imaging

The joint inversion of the P- and S-wave phase arrivals for hypocenter locations and 3D velocity structure was performed with the inversion code tomoFDD (Zhang and Thurber, 2003; Gritto et al., 2013a,b), which was upgraded from its original version to account for dynamic memory allocation. The addition of dynamic memory allocation and the use of tomoFDD's fast finite difference eikonal solver (Podvin and Lecomte, 1991) make the code well suited for the situation at The Geysers, where the combination of a high number of stations, a high volume of recorded earthquake data and a high number of inversion nodes pose great demands on computer memory and CPU speed.

The 3D inversion of the P- and S-wave phase arrival times for the 17,000 events resulted in the misfit functions presented in Figure 6. The curves represent the misfit between observed and calculated travel times as a function of iteration. The separate curves depict the misfit of the absolute mean, the weighted mean, the absolute variance and the weighted variance of the travel times. The curves decrease with increasing number of iterations indicating that the misfit is successively minimized until it does not change any further and the inversion is stopped as a smoothness constraint for the resulting velocity models.

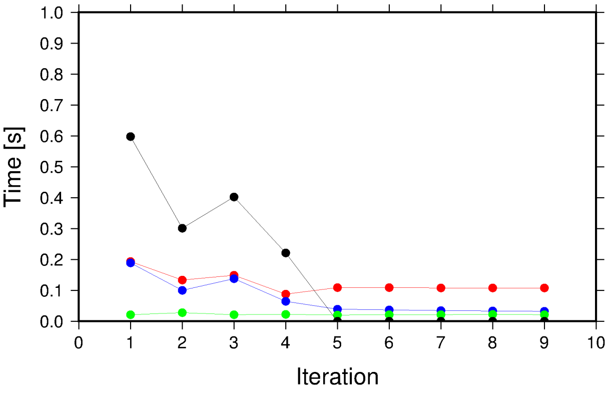

Figure 6: Misfit between synthetic and observed travel times as a function of iterations. Black: misfit of weighted variance. Red: misfit of absolute mean. Blue: misfit of weighted mean. Green: misfit of absolute variance.

The P-wave velocity estimates for a selection of horizontal depth slices are presented in Figures 7a. The velocity estimates are only plotted for nodes that have sufficient resolution as defined by the derivative weight sum (DWS), which represents a measure of the ray density at each node. Areas with insufficient resolution are plotted white. The resolution is highest in the central part and at central depths of the reservoir because of the high number of recorded seismic events and decreases slightly in the shallow part of the reservoir, in the deeper sections of the reservoir and towards the boundaries of the study area. The shallow parts of the reservoir exhibit intermediate P-wave velocities between Vp = 4.5 - 5.5 km/s, with lower values in the north-west and higher values in the south-east of the study area. These estimates increase with depth until maximum velocity values of Vp = 6.3 km/s are observed in the central part of the study area surrounded by lower velocity values of Vp < 5.5 km/s. An interpretation of the velocity estimates will be given at the end of this section.

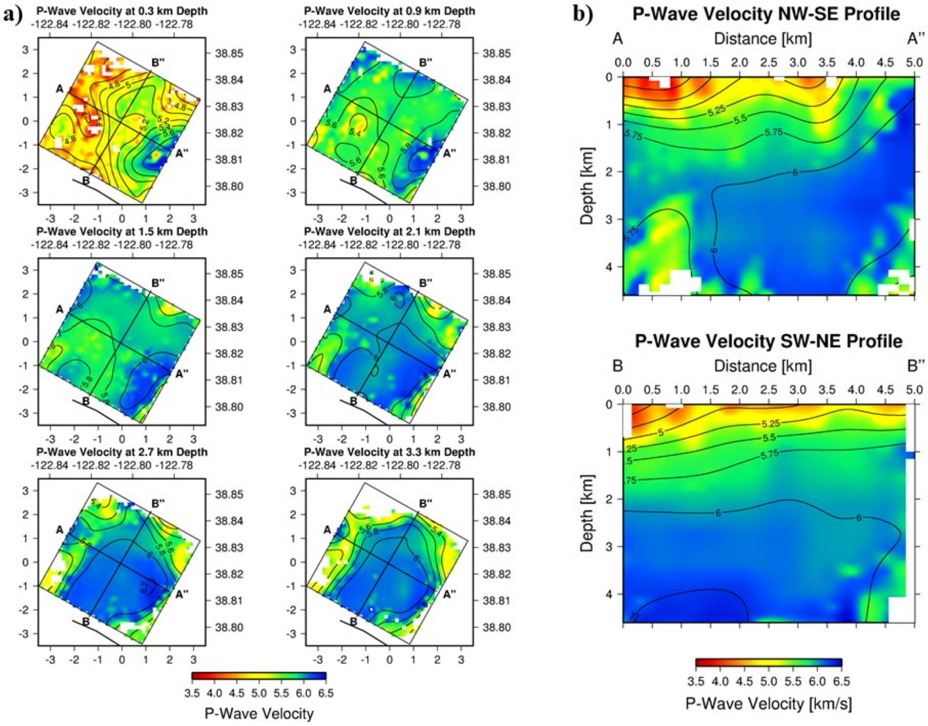

Figure 7: a) Horizontal slices of the P-wave velocity estimates for the reservoir structure from travel time inversion of 17,000 events. The estimates are only shown for regions that have sufficient ray coverage as determined by the derivative weight sum (DWS). The depth of the horizontal slices are denoted at the top of each panel. b) Vertical cross-sections of the P-wave velocity estimates along profiles A-A" and B-B" in Figure 7a.

The vertical cross-sections along the profiles denoted A-A" and B-B" in Figure 7a are displayed in Figure 7b. The cross-section trending from north-west to south-east (Figure 7b, top) reveals low velocity values between Vp = 3.5 - 4.5 km/s in the uppermost section of the reservoir. A high velocity anomaly with values above Vp = 6.0 km/s is seen dipping from shallower depth in the south-east to greater depth in the center of the study area. It is bounded by a lower velocity body (Vp = 5.0 - 5.5 km/s) towards the north-west. This is the same low-velocity structure that is surrounding the high velocity anomaly in Figure 7a at 2.7 and 3.3 km depth. The cross-section trending from south-west to north-east (Figure 7b, bottom) reveals the same low velocity anomaly with values above Vp = 6.25 km/s in the south-west, while lower velocities are observed towards the north-east.

The inversion estimates for the S-wave velocity structure below the study area are presented in Figures 8a, for the same selection of horizontal depth slices as for the P-wave velocity. Again, velocity estimates are only plotted for nodes that have sufficient resolution such as in regions with high seismicity. Because the number of S-wave picks is lower than that of the P-wave picks, the resolution of the S-wave velocity estimates is decreased relative to the P-wave resolution in Figure 7. However, the spatial distribution of the S-wave velocities is similar to that of the P-wave velocities. In the shallow parts of the reservoir S-wave velocities between Vs = 2.5 - 3.2 km/s are observed, with lower values in the north-west and higher values in the south-east of the study area. As before, these estimates increase with depth until maximum velocity values of Vs = 3.8 km/s are observed in the central part of the study area. Overall, the S-wave velocity distribution in horizontal and vertical direction is similar to that of the P-wave velocity structure in Figure 7a.

The vertical cross-sections along the profiles denoted A-A" and B-B" in Figure 8a are displayed in Figure 8b. The cross-section trending from north-west to south-east (Figure 8b, top) reveals low velocity values between Vs = 2.3-2.7 km/s in the uppermost section of the reservoir. The high velocity anomaly, encountered in the P-wave velocity structure, is visible again dipping from shallower depth in the south-east to greater depth in the center of the study area with values of Vs = 3.75 km/s. In the perpendicular direction (south-west to north-east, Figure 8b bottom), this high velocity anomaly is located centrally at depth of approximately 4 km.

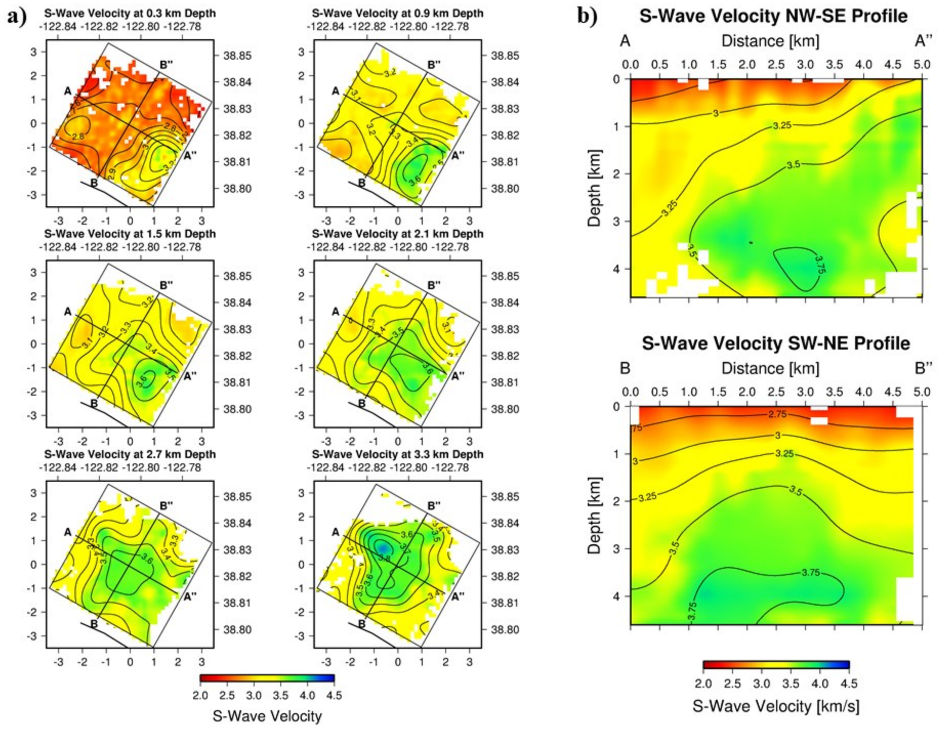

Figure 8: a) Horizontal slices of the S-wave velocity estimates for the reservoir structure from travel time inversion of 17,000 events. The estimates are only shown for regions that have sufficient ray coverage as determined by the derivative weight sum (DWS). The depth of the horizontal slices are denoted at the top of each panel. b) Vertical cross-sections of the S-wave velocity estimates along profiles A-A" and B-B" in Figure 8a.

A possible interpretation of the velocity structure shown in Figures 7 and 8 is given by the major geological formations in The Geysers, consisting of sheared and fractured graywacke interspersed with greenstone in the shallower parts of the reservoir, which are underlain by felsite, a granitic intrusion into the reservoir. The surface representing the top of the felsite is shown in Figure 9. The felsite structure has its shallowest part in the southeast Geysers and dips towards the northwest. The high-velocity felsite is the most likely cause for the southeast-to-northwest dipping high-velocity structure visible in the tomographic images in Figures 7 and 8. Similarly, the metamorphosed graywacke formation in the shallower part of the reservoir is represented by the intermediate-velocity structures.

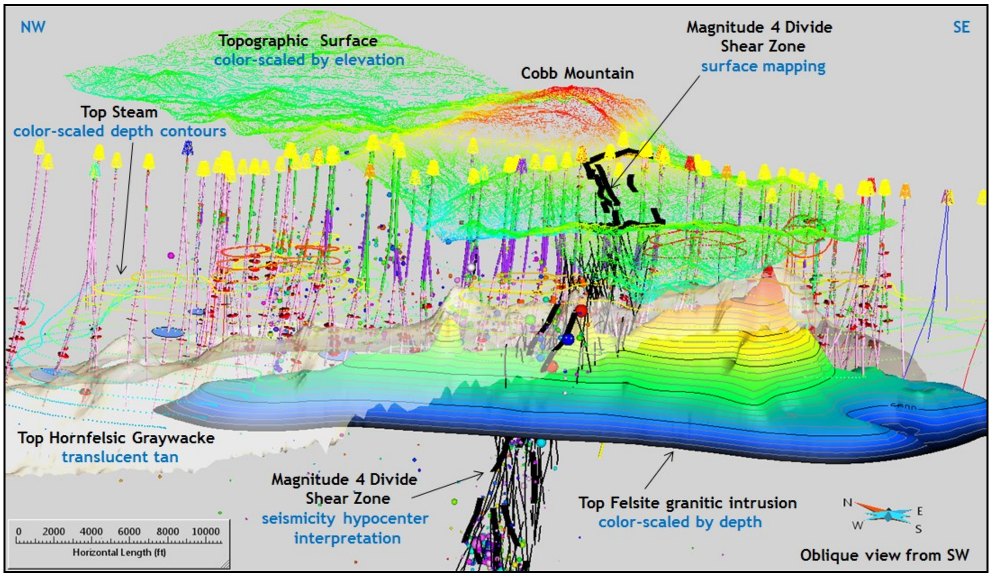

Figure 9: The Geysers 3D structural model denoting the top interface of the Felsite granitic intrusion as view from SW. The vertical lineaments denote injection and production wells (from Hartline et al., 2016).

4.2 Vp/Vs-Ratio Imaging

While estimates of the P- and S-wave velocity are useful to delineate the geological structure of the reservoir, the Vp/Vs-ratio is well suited to estimate gas and liquid fluid saturation. Applications include imaging fluids such as oil, water and CO_2 in second and tertiary oil recovery (Gritto et al., 2004), tracing the movement of fluids associated with volcanic swarms (Dahm and Fischer, 2013), imaging fluids in fault zones (Lin and Shearer, 2007) and mapping the presence of liquid and gaseous fluids in geothermal reservoirs (Julian et al., 1996; Lin and Shearer, 2009; Gritto et al., 2013a,b; Gritto and Jarpe, 2014). In the present study, we calculated the Vp/Vs-ratio from the P- and S-wave velocity estimates obtained from the travel time inversion. The inversion estimates for the Vp/Vs-ratio are presented in Figure 10, for the same selection of horizontal depth slices as before. Because Vp/Vs-ratio is computed by taking the ratio of the P-wave and S-wave velocity estimates, the resolution of the Vp/Vs estimates is taken from the S-wave resolution, as it is lower than the P-wave resolution. The results in Figure 10a indicate that low Vp/Vs-ratios (1.4) can be found in the shallow parts of the reservoir in the north-west, while high Vp/Vs-ratios (2.0) can be seen in the north-east. These may be indicative of steam and water saturated areas, respectively, and may be related to injection and production activities. With increasing depth, the Vp/Vs-ratio drops to values around Vp/Vs = 1.55 - 1.65 as can be expected for a steam dominated reservoir, such as The Geysers. The vertical cross-sections in Figure 10b reveal at shallow depth the low Vp/Vs estimates in the north-western region of the study area and the high Vp/Vs estimates in the north-eastern region. They also display a high Vp/Vs region along the north-western boundary of the study area at a depth of ~ 1.5 - 2.5 km. The low Vp/Vs anomaly (< 1.65) is visible in the central parts of the study area between 3 - 4 km depth.

The overall structure of the Vp/Vs-ratio is noticeably different from the Vp and Vs estimates in Figures 7 and 8. The Vp/Vs images reveal more heterogeneity within the reservoir, which is related to water injection and steam production operations, as we will show in the next section.

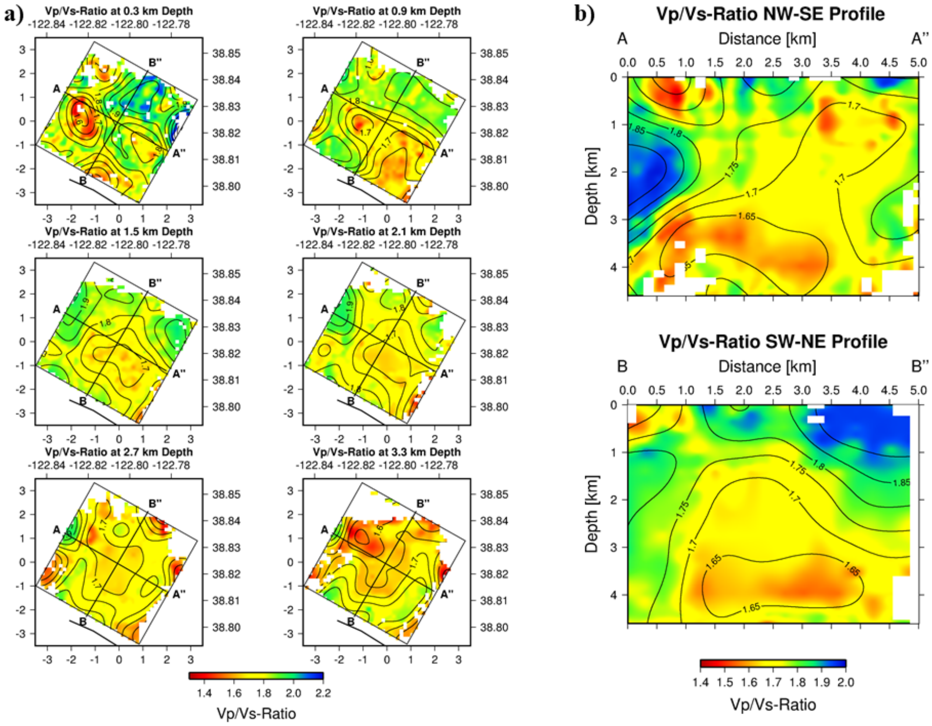

Figure 10: a) Horizontal slices of the Vp/Vs estimates for the reservoir structure from travel time inversion of 17,000 events. The estimates are only shown for regions that have sufficient ray coverage as determined by the derivative weight sum (DWS). The depth of the horizontal slices are denoted at the top of each panel. b) Vertical cross-sections of the Vp/Vs estimates along profiles A-A" and B-B" in Figure 9a.

5. CORRELATION OF SEISMIC IMAGING RESULTS TO INJECTION AND PRODUCTION ACTIVITIES

5.1 Correlation of P- and S-Wave Velocity to Injection and Production Activities

Over the past decade, Calpine Corporation has developed a three-dimensional structural model of The Geysers geothermal field using Paradigm Geophysical SKUA GOCAD software. Structural model building constraints include lithology logs, surface geologic maps earthquake hypocenters as well as borehole trajectories, temperature logs, pressure logs, tracer analysis patterns, heat flow patterns, water injection, steam production, reservoir interfaces and reservoir history matching (Hartline et al., 2016). A scaled-down version of the 3D reservoir model was made available to the current project to help correlate the geophysical results, including earthquake hypocenters and velocity images to reservoir interfaces, water injection and steam production volumes among others. The ultimate goal is to support Calpine with their operations and with planning and designing of their borehole drilling program.

A 3D example of the 3D P- wave and S-wave velocity models and water injection and steam production wells is provided in Figure 11. The type of wells in this figure can be distinguished by their total depth, with water injection wells reaching greater depth, while steam production wells are generally shallower. Figure 10a displays the P-wave velocity model, which indicates a velocity gradient with lower velocities in the near surface (orange), intermediate velocities below (green) and high velocities (blue) in the deeper region of the reservoir, which is consistent with the results shown in Figure 7 and 8 and is a representation of the major geological formations in the reservoir. However, a closer inspection of the velocity estimates in the vicinity of the steam production wells reveals a “pull-down” of the lower velocities (orange) to intermediate reservoir depth. This could be an indication for the steam saturation surrounding the production wells in this part of the reservoir. Conversely, the velocity estimates in the vicinity of the water injection wells reveal a “pull-up” of the higher velocities (blue) to intermediate reservoir depth. The water injection wells have open-hole sections along the borehole, which allows water to flow into the reservoir rock. These velocity anomalies could be an indication for an increase in water saturation in the vicinity and below the water injection wells. In contrast, Figure 10b, which displays the S-wave velocity model does not show a strong correlation with the water injection and steam production wells, as can be expected considering the properties of shear waves, which are much less sensitive to fluid saturation in the subsurface. The example shows that the 3D velocity model can be used for geological and structural interpretation as well as for delineation of the heterogeneity in water and steam saturation.

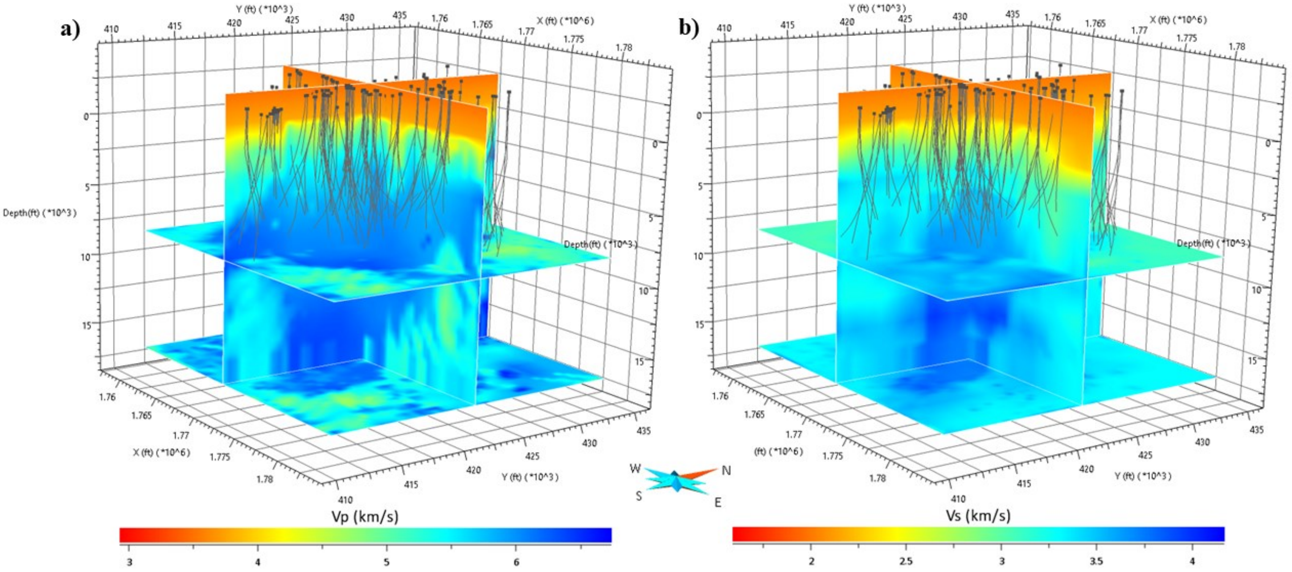

Figure 11: a) Fence diagram through the 3D P-wave velocity model with water injection (deep) and steam production (shallow) wells superimposed. b) Fence diagram through the 3D S-wave velocity model with water injection (deep) and steam production (shallow) wells superimposed.

5.2 Correlation of Vp/Vs-Ratio to Injection and Production Activities

In section 4.2, it was shown that the Vp/Vs-ratio reveals a higher degree of heterogeneity within the reservoir, which is related to water injection and steam production operations. This concept is shown in Figure 12, which presents a map view of the Vp/Vs-ratio at 700 m depth (Figure 12a) and related fence diagrams view views from south-east (Figure 12b) and from south-west (Figure 12c). For the purpose of improved visualization, a group of injection wells in the western part of the study area was selected for correlation to the Vp/Vs-ratio. Steam entries in the 3D reservoir model are represented by discs that transect the well trajectory orthogonally at the depth of the steam encounter. The size of the disc is proportional to the steam pressure encountered at that depth. The Vp/Vs-ratio in Figure 12a shows a low anomaly (Vp/Vs ~ 1.5) in the vicinity of the steam production well, which is indicated by the round disc. The Vp/Vs anomaly appears extensive at this depth level extending outward from the production well. Additional perspectives are provided by the fence diagrams in Figures 12b,c, where the group of selected steam production wells are indicated by their trajectories through the 3D model. The largest steam entry disc is partially obscured by the vertical sections, as they are centered on the location of the steam entry in the well. Nevertheless, is can be seen that the steam entry correlates very well with the low Vp/Vs anomaly surrounding this well. A closer inspection of Figure 12c reveals that the group of wells in the south-western most corner of the study area also displays steam entries that correlate well with low Vp/Vs anomalies. However, the steam entries and Vp/Vs anomalies are smaller than in the previous example. While this is only the beginning of our analysis to investigate spatial correlation of Vp/Vs-ratio to water injection and steam production operations, the example shows that there is promise of using this seismic property to delineate liquids in the reservoir.

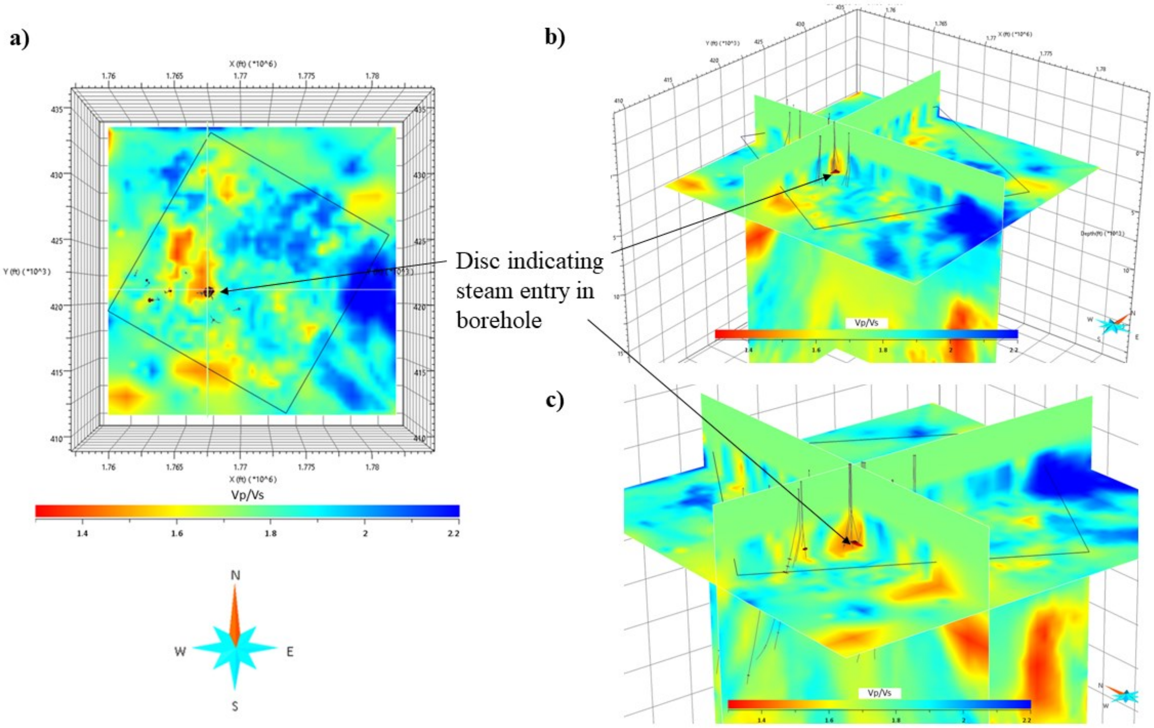

Disc indicating steam entry in borehole

Figure 12: a) Map view of the Vp/Vs-ratio at 700 m depth. The back square denotes the study area, while the black lines in the western part of the image are projections of the well trajectories of a group of injection wells. b) Fence diagram through the Vp/Vs model with a group of steam production wells superimposed. The small red symbols cutting orthogonally through the well trajectories represent the volume of steam encountered in the well. View from south-east. c) Fence diagram through the Vp/Vs model with a group of steam production wells superimposed. The small red symbols cutting orthogonally through the well trajectories represent the volume of steam encountered in the well. View from south-west.

6. CONCLUSIONS

The development of inexpensive seismic recording systems has led to the use of passive seismic networks with dense station coverage to investigate shallow and deeper structures of the Earth's crust. While in the past, this technique has mainly been used in the oil and gas industry, the cost-effectiveness of this capability makes it more appealing to the geothermal industry in recent years. The current project is designed to conduct high-resolution passive seismic imaging at The Geysers to support reservoir operations in an area that has been selected for future development. The high seismicity rate in the reservoir helps to improve the resolution and the reliability of the velocity estimates obtained from 3D inversion of seismic data. The derived 3D P- and S-wave velocity models can be used to delineate major geological formations in The Geysers and help to support the development of the 3D reservoir model. Moreover, the 3D model of Vp/Vs-ratio, derived from the Vp and Vs estimates, shows promise in delineating regions with steam or water concentration throughout the reservoir. This makes passive seismic imaging an appealing technique to support the development of a drilling program and to support geothermal operations to optimize the use of the resource in general.

REFERENCES

Bowden, D.C., V.C. Tsai, and F.-C. Lin, (2015), Site amplification, attenuation, and scattering from noise correlation amplitudes across a dense array in Long Beach, CA, *Geophys. Res. Lett*., **42**, 1360–1367, doi:10.1002/2014GL062662.

FairfieldNodal, http://www.fairfieldnodal.com/.

Dahm, T. and T. Fischer: Velocity ratio variations in the source region of earthquake swarms in NW Bohemia obtained from arrival time double-differences, *Geophys J. Int*., Volume 196, Issue 2, February, 2014, Pages 957–970, doi: 10.1093/gji/ggt410., (2013).

Gritto, R.; Daley, T.M., and Myer, L.R.: Joint Cross Well and Single Well Seismic Studies of CO2 Injection in an Oil Reservoir, *Geophysical Prospecting*, Vol. 52, pp. 323-339, (2004).

Gritto, R., S.-H. Yoo and S.P. Jarpe: Three-dimensional seismic tomography at The Geysers geothermal field, CA, USA, *Proceedings,* 38th Workshop Geothermal Reservoir Engineering, SGP-TR-198, (2013a).

Gritto, R., S.H. Yoo and S.P. Jarpe: Seismic Imaging of reservoir structure at The Geysers geothermal reservoir, *Proceedings,* AGU 2013 Fall Meeting, S33D-2460, San Francisco, USA, 9–13 December 2013, (2013b).

Gritto, R. and S.P. Jarpe: Temporal variations of Vp/Vs-ratio at The Geysers geothermal field, USA, *Geothermics*, http://dx.doi.org/10.1016/j.geothermics.2014.01.012, (2014).

Gritto, R., D.W. Vasco, L.J. Hutchings and K.T. Nihei: High-Resolution Seismic Imaging of a Geothermal Reservoir Using a Cost-Effective Dense Seismic Network, *Proceedings,* 44th Workshop on Geothermal Reservoir Engineering, Stanford University, Stanford, CA, (2019).

Hartline, C.S., M.A. Walters, M.C. Wright, C.K. Forson, and A.J. Sadowski: Three-Dimensional Structural Model Building, Induced Seismicity Analysis, Drilling Analysis and Reservoir Management at The Geysers Geothermal Field, Northern California, *Proceedings*, 41st Workshop on Geothermal Reservoir Engineering, Stanford University, Stanford, California, February 22-24, SGP-TR-209, (2016).

Layland-Bachmann, C.E., R. Gritto, C.S. Hartline, L.J. Hutchings., S.R. Jarpe, K.T. Nihei and M. Schoenball: In-depth Analysis from Deployments of Low-Cost Seismic Instruments in the Geysers Geothermal Field, *Proceedings,* AGU 2019 Fall Meeting, San Francisco, CA, Dec. 9-13, S11F-0394, (2019).

Lehujeur, M, J. Vergne, J. Schmittbuhl, D. Zigone and A. Le Chenadec: Reservoir Imaging Using Ambient Noise Correlation from a Dense Seismic Network, *J. Geophys. Res*., 123, 8, 6671-6686, (2018).

Lin, F.-C., D. Li, R.W. Clayton, and D. Hollis: High-resolution 3D shallow crustal structure in Long Beach, California: Application of ambient noise tomography on a dense seismic array, *Geophys*., **78**(4), Q45–Q56, doi: 10.1190/GEO2012-0453.1, (2013).

MicroSeismic, http://www.microseismic.com/.

Nakata, N., J. Chang, J.F. Lawrence, and P. Boué: Body wave extraction and tomography at Long Beach, California, using ambient noise interferometery, *J. Geophys. Res*., **120**, 1159-1173, doi: 10.1002/2015JB011870, (2015).

NodalSeismic, www.nodalseismic.com/.

Podvin, P., and I. Lecomte: Finite difference computation of travel times in very contrasted velocity models: A massively parallel approach and its associated tools, *Geophys. J. Int*., **105**, 271–284, (1991).

Wang, Y, F.- C., Lin, B., Schmandt, J., Farrell: Ambient noise tomography across Mount St. Helens using a dense seismic array, *J. Geophys. Res*., **122**, 1159-1173, https://doi.org/10.1002/2016JB013769, (2017).

Zhang, H. and C. H. Thurber: Double-Difference Tomography: The Method and Its Application to the Hayward Fault, California, *Bull. Seis. Soc. Am.*, **93**, 1875-1889, (2003).

ACKNOWLEDGEMENT

This work was supported by the California Energy Commission under Contract No. EPC-16-021. The authors would like to thank Calpine Corporation for access to the field, Ramsey Haught for his help in testing and installing the seismic recording sytems and Florian Soom for collecting the seismic data in the field.